Effect of Hf and Ta on creep deformation behaviors of PM Ni-based superalloys

Hao-peng ZHANG[1,2], Jia-ming BAI[1,2,3], Xin-yu LI[1,2,3], Xiao-kun LI[1,2], Jian JIA[1,2], Jian-tao LIU[1,2], Yi-wen ZHANG[1,2]

1. High Temperature Material Research Institute, Central Iron and Steel Research Institute, Beijing 100081, China;
2. Gaona Aero Material Co., Ltd., Beijing 100081, China;
3. School of Materials Science and Engineering, Northeastern University, Shenyang 110819, China

Abstract: Four powder metallurgy (PM) Ni-based superalloys with different Hf and Ta contents were creep-tested at 650 °C and 970 MPa, 700 °C and 770 MPa, and 750 °C and 580 MPa, respectively. The effect of Hf and Ta on creep deformation behaviors of the superalloys was studied from multiple scales by SEM, electron backscatter diffraction (EBSD), and aberration-corrected scanning transmission electron microscope (AC-STEM). The results showed that Hf and Ta suppressed the intergranular fracture and initiation of cracks during the acceleration creep stage, which prolonged the creep rupture time. Hf and Ta inhibited the stacking faults extending and the dislocation climbing and promoted the Suzuki segregation of W during the steady-state creep stage, which reduced the minimum creep rate and delayed the start time of the acceleration creep stage. The Suzuki segregation of Co, Cr, Mo, Ti, Nb, W, and Ta along stacking faults was observed after Hf and Ta addition, leading to the localized phase transformation in the γ' phase, and the stacking fault phase was chemically disordered. This study provided ideas for the composition design of novel PM Ni-based superalloys and theoretical foundations for the combined addition of Hf and Ta.

Key words: PM Ni-based superalloy; Hf; Ta; creep deformation behaviors; Suzuki segregation

1 Introduction

Powder metallurgy (PM) Ni-based superalloys are one of the most crucial high-temperature structural materials in turbine disks of high-performance aero-engines [1,2]. Due to limiting the composition segregation within the range of powder size, PM Ni-based superalloys can effectively eliminate the macroscopic segregation and ensure microstructure homogeneity [3]. To further improve the thrust-weight ratio and the fuel utilization of aero-engines, it is necessary to increase the turbine inlet temperature, thereby providing a higher requirement on the temperature capability of PM Ni-based superalloys. Therefore, how to optimize the alloy composition and design novel PM Ni-based superalloys has become one of the research hotspots [4,5].

Hf and Ta have been added to PM Ni-based superalloys for a long time to enhance the microstructure and mechanical properties. In the second-generation PM Ni-based superalloys, 0.5 Hf (wt.%, the same below) was added to the N18. In the third-generation PM Ni-based superalloys, 2.4 Ta was added to the René104, 0.9 Ta was added to the Alloy 10, 0.3 Hf was added to the N19, and 0.5Hf+2.0Ta was added to the RR1000 [6]. In the fourth-generation PM Ni-based superalloys, the combined addition of Hf and Ta has become more common, and the addition amount has been further increased, such as adding 0.4Hf+4.8Ta in the

ME501 [7], 0.37Hf+4.8Ta in the TSNA-1 [8], 0.36Hf+3.0Ta in the RRHT3, and 0.42Hf+3.0Ta in the RRHT4 [9]. It can be seen that the combined addition of Hf and Ta has become one of the trends in the composition design of novel PM Ni-based superalloys. Therefore, studying the effect of the combined addition of Hf and Ta has significant practical significance.

The effect of Hf and Ta on the microstructure, tensile behaviors, creep rupture characteristics, and properties of the PM-Ni-based superalloys was reported in our previous studies [6,10,11]. However, there are few studies on the effect of Hf and Ta on creep deformation behaviors. Previous studies mainly focused on the effect of Hf or Ta on creep properties. For example, as early as 1961, COCHARDT [12] found that adding 0.5Hf significantly improved creep rupture properties. The rupture time was increased from 868 to 1246 h and the rupture elongation was increased from 7.2% to 13% after creep at 730 °C and 207 MPa. ZHAO et al [13] reported that adding 0.4 Hf prolonged the creep life and reduced the minimum creep rate after creep at 1100 °C and 130 MPa. ZHANG and HU [14] found that adding 0.3 Hf improved the creep resistance after creep at 750 °C and 460 MPa, and eliminated notch sensitivity after creep at 650 °C and 1020 MPa. YANG et al [15] reported that adding 2.4 Ta reduced the steady-state creep rate and prolonged the steady-state creep time from 75 to 240 h and creep rupture time from 140 to 370 h after creep at 750 °C and 600 MPa. BAI et al [16] further reported that adding 2.4 Ta also significantly reduced the minimum creep rate and prolonged creep rupture time after creep at 650 °C and 980 MPa, 700 °C and 770 MPa, and 800 °C and 400 MPa, respectively. By comparing the Larson−Miller parameter curves, it was found that adding 2.4 Ta increased the operating temperature by 23 °C after serving for 500 h at the stress of 1000 MPa, and by 15 °C after serving for 500 h at the stress of 550 MPa. However, the effect of the combined addition of Hf and Ta on the creep deformation behaviors is still unclear, and the mechanism behind this effect is even less clear.

This study focused on four experimental alloys with only Hf and Ta content changes and systematically investigated the effects of Hf and Ta on creep deformation behaviors under different creep conditions. The microstructure changes, deformation substructures, and Suzuki segregation were investigated by advanced characterization methods, and the action mechanisms of the Hf and Ta were discussed. This work is expected to provide some ideas for optimizing alloy composition and support the research of novel PM Ni-based superalloys.

2 Experimental

The nominal mass fractions of Hf and Ta in four experimental PM Ni-based superalloys were 0Hf+0Ta, 0.5Hf+0Ta, 0Hf+2.4Ta, and 0.5Hf+2.4Ta, respectively. The actual compositions of four alloys are listed in Table 1. The experimental alloys were prepared by the PM process, which included producing powders by plasma rotating electrode process (PREP), sieving powders to obtain 50−150 μm alloy powders, and loading the powders into cans for hot isostatic pressing (HIP) at 1200 °C, 120 MPa and 4 h. The heat treatment (HT) included a supersolvus heat treatment of (1180 °C, 2 h) + 600 °C salt bath for 30 min + air cooling (AC) and an aging treatment of (760 °C, 16 h) + AC. The creep test conditions included 650 °C and 970 MPa, 700 °C and 770 MPa, and 750 °C and 580 MPa. The creep samples had cylindrical gauge sections of d5 mm × 25 mm.

The microstructure characterization was carried out using the Olympus GX71 optical microscope

Table 1 Actual compositions of experimental PM Ni-based superalloys (wt.%)

Alloy	Cr	Co	W	Mo	Al	Ti	Nb	C	B	Zr	Hf	Ta	Ni
0Hf+0Ta	15.7	12.9	4.0	4.1	2.2	3.9	0.8	0.05	0.01	0.04	0	0	Bal.
0.5Hf+0Ta	15.6	12.9	4.0	4.1	2.2	3.9	0.9	0.05	0.01	0.04	0.52	0	Bal.
0Hf+2.4Ta	15.6	13.2	4.0	4.0	2.3	3.9	0.8	0.06	0.01	0.04	0	2.41	Bal.
0.5Hf+2.4Ta	15.7	13.2	4.0	4.0	2.4	3.9	0.8	0.06	0.01	0.04	0.52	2.40	Bal.

(OM), JEOL JSM−7200F field emission scanning electron microscope (FE-SEM) equipped with Oxford Symmetry S2 electron backscatter diffraction (EBSD) detector operated at 5−20 kV, and FEI Themis Z aberration-corrected scanning transmission electron microscope (AC-STEM) equipped with 4 in-column SDD Super-X energy dispersive X-ray spectroscopy (EDS) detectors operated at 300 kV. OM samples were prepared by chemical etching with 20 g $CuCl_2$ + 100 mL HCl + 100 mL C_2H_5OH for 15 s. SEM samples were prepared by electrolytic polishing with 20% H_2SO_4 + 80% CH_3OH at 20 V for 10 s, and electrolytic etching with 30 mL H_3PO_4 + 3 g CrO_3 + 2 mL H_2SO_4 at 5 V for 2 s. EBSD samples were prepared by electrolytic polishing with 20% H_2SO_4 + 80% CH_3OH at 20 V for 5 s. TEM foils were extracted from gauges oriented 45° to the stress axis to investigate deformation along crystallographic planes edge-on. TEM samples were prepared by twin-jet electropolishing with 10% $HClO_4$ + 90% C_2H_5OH at −25 °C and 80 mA.

3 Results

3.1 Microstructures of HT alloy

Figure 1 exhibits the microstructures of HT experimental alloys. As shown in Figs. 1(a_1−a_4), the addition of Hf and Ta has little effect on the grain size which is about 40 μm, but significantly suppresses the prior particle boundaries (PPBs), which are indicated by arrows in Fig. 1(a_1). Figures 1(b_1−b_4) show the morphology of γ' particles. Due to the supersolvus HT, there are few primary γ' precipitates. Hf and Ta have little effect on tertiary γ' precipitates, but significantly change the secondary γ' precipitates. Compared with 0Hf+0Ta alloy, the volume fraction of secondary γ' precipitates in 0.5Hf+2.4Ta alloy is increased from 40% to 45%, the equivalent size of secondary γ' precipitates is increased from 130 to 180 nm, and their shapes change from spherical to cubic and petal shaped [10].

3.2 Creep curves and creep performances

A typical creep curve of PM Ni-based superalloys can be divided into three stages according to the variation of creep rate: (I) the deceleration stage, (II) the steady-state stage, and (III) the acceleration stage. Figure 2 shows an example of 0Hf+2.4Ta alloy after creep at 650 °C and 970 MPa. To divide the three stages more accurately, the first and second derivatives of the creep strain are plotted in Fig. 2(a). The stage where the second derivative of strain is approximately 0 and the first derivative of strain (i.e., creep rate) is approximately constant is divided into the steady-state stage. Figure 2(b) shows the creep curve after dividing into three stages, and it can be seen that the steady-state stage is approximately a straight line.
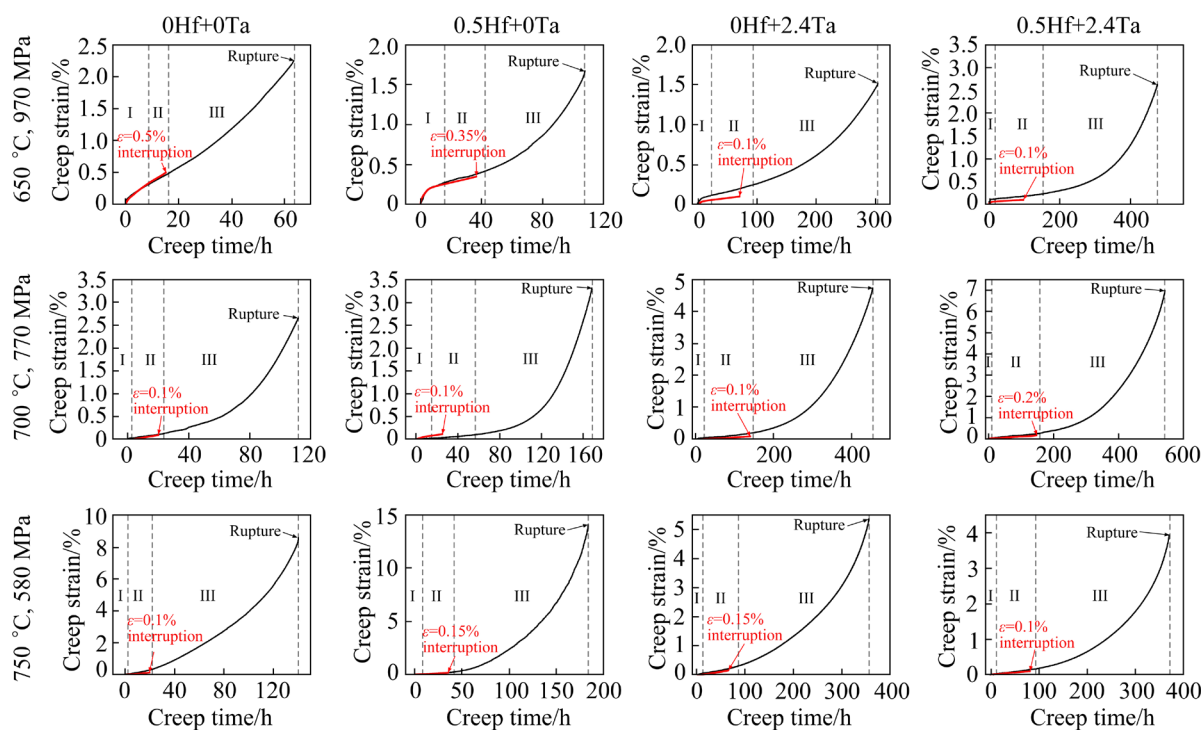
According to the above method, creep curves of the 0Hf+0Ta, 0.5Hf+0Ta, 0Hf+2.4Ta, and 0.5Hf+2.4Ta alloys after creep at 650 °C and 970 MPa, 700 °C and 770 MPa, and 750 °C and 580 MPa are plotted in Fig. 3, and three creep stages are divided. The addition of Hf and Ta obviously increases the creep rupture time. However, regardless of the addition of Hf and Ta, the durations of the deceleration stages and steady-
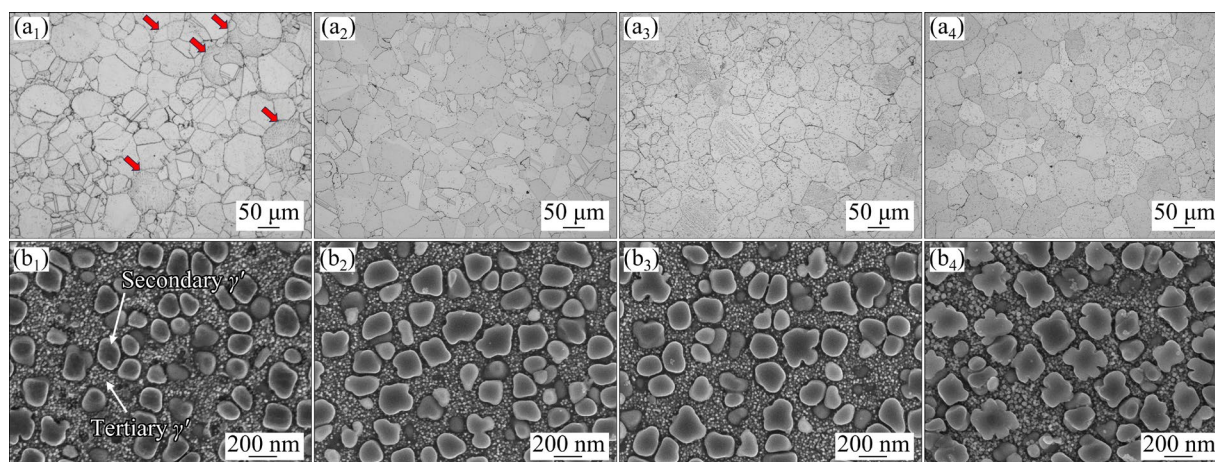
Fig. 1 OM (a_1−a_4) and SEM (b_1−b_4) images of HT alloys: (a_1, b_1) 0Hf+0Ta; (a_2, b_2) 0.5Hf+0Ta; (a_3, b_3) 0Hf+2.4Ta; (a_4, b_4) 0.5Hf+2.4Ta
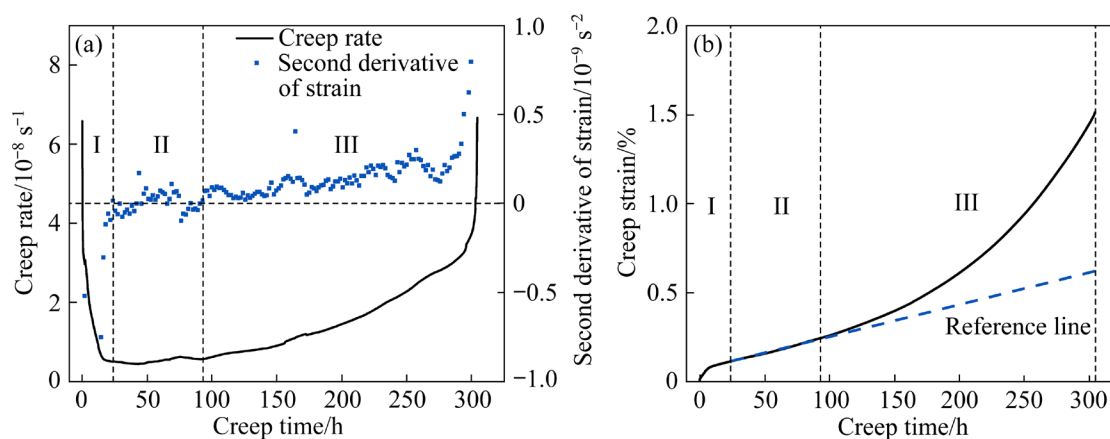
Fig. 2 Schematic diagrams of 0Hf+2.4Ta after creep at 650 °C and 970 MPa showing division of creep stages: (a) Creep rate (the first derivative of creep strain with respect to creep time) and second derivative of creep strain with respect to creep time; (b) Creep curve


Fig. 3 Creep curves (black) and creep interruption curves (red) of 0Hf+0Ta, 0.5Hf+0Ta, 0Hf+2.4Ta, and 0.5Hf+2.4Ta alloys after creep at 650 °C and 970 MPa, 700 °C and 770 MPa, and 750 °C and 580 MPa (The creep interruption strain is marked in the figures)

state stages are all relatively short, while acceleration stages are all relatively long due to the high damage tolerance of the alloy. Because the creep strain increases rapidly in the acceleration stage, the deformation in the acceleration stage is always not allowed for engineering specimens in practice, so the research on the deformation in the steady-state stage has greater engineering significance. Therefore, creep interruption tests

interrupted in the steady-state stage were conducted by the time control. The creep interruption curves are shown in Fig. 3 in red curves. Although experimental errors result in two kinds of curves without completely overlapping, the three separate creep stages are still applicable.

To demonstrate the effects of Hf and Ta on the creep performances more clearly, Fig. 4 shows quantitative creep performances of experimental
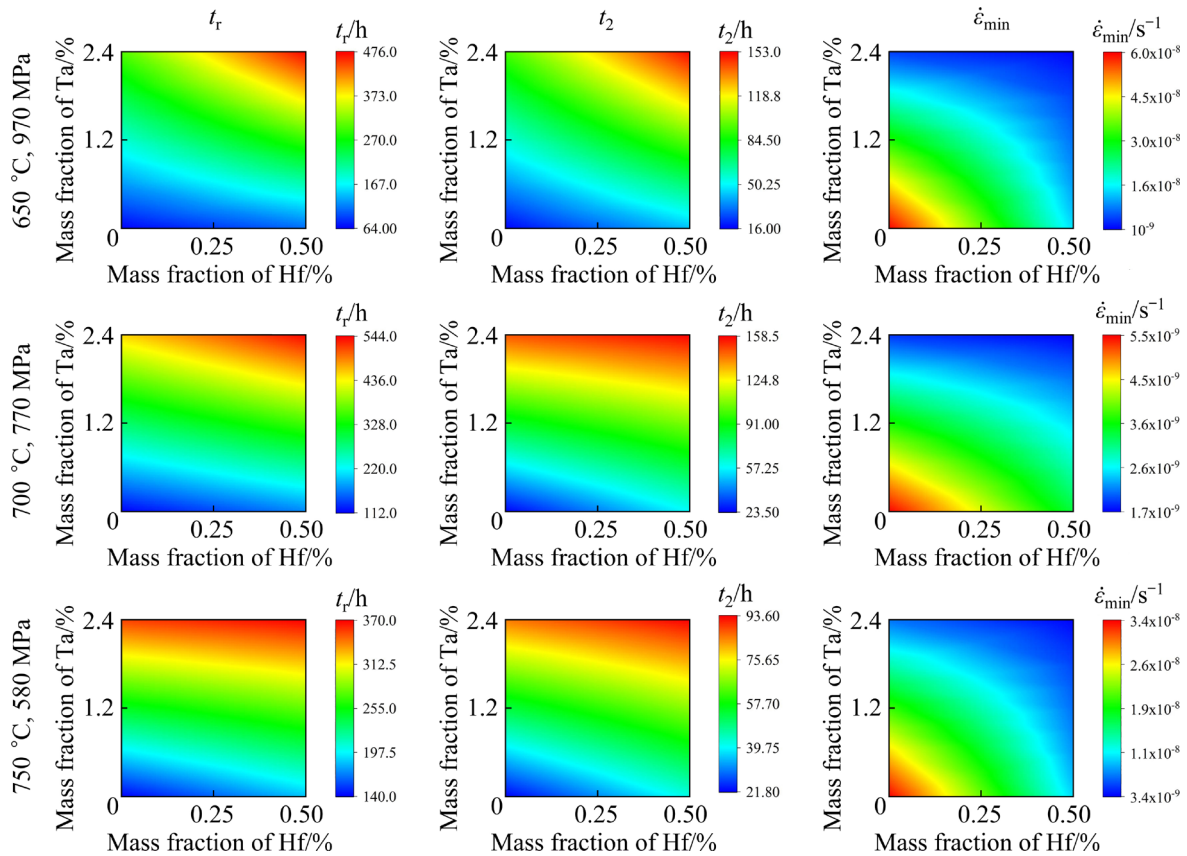
Fig. 4 Effect of Hf and Ta addition on creep rupture time (t_r), start time of acceleration creep stage (t_2), and minimum creep rate ($\dot{\varepsilon}_{\min}$)

alloys in the form of contour maps, where the horizontal and vertical coordinates are the Hf and Ta contents, respectively. It can be clearly seen that Hf and Ta prolong the creep rupture time (t_r), delay the start time of the acceleration creep stage (t_2, i.e., the end time of the steady-state creep stage), and decrease the minimum creep rate ($\dot{\varepsilon}_{\min}$) under all creep conditions. Therefore, the addition of Hf and Ta significantly enhances the creep performances.

3.3 Creep fractures and morphological changes of γ' phase

Figure 5 shows the creep fractures of 0Hf+0Ta and 0.5Hf+2.4Ta alloys. The crack source area (CSA) shows a typical intergranular fracture, and the crack propagation area (CPA) shows a mixture of intergranular and transgranular fracture, which indicates that the intergranular damage is the main cause of creep rupture. The area fraction of CSA is statistically analyzed, and it increases with the increase of temperature and decreases with the increase of addition of Hf and Ta. This shows that

high temperature promotes intergranular fracture, while the addition of Hf and Ta suppresses intergranular fracture in the acceleration creep stage.

Figure 6 shows the morphologies of γ' phase of 0Hf+0Ta and 0.5Hf+2.4Ta alloys after creep interruption and creep rupture. Firstly, compared to creep interruption, the size of the secondary γ' phase increases and its shape becomes more split after creep rupture. This indicates that the high temperature and stress during creep promote secondary γ' particles coarsening and splitting. Secondly, the quantity of tertiary γ' particles significantly decreases after creep interruption at 750 °C and 580 MPa, and tertiary γ' particles almost disappear after creep rupture at 750 °C and 580 MPa. This indicates that during the creep at 750 °C and 580 MPa, tertiary γ' particles are gradually dissolving. It is worth noting that due to the differences in creep interruption and rupture time, the effects of Hf and Ta on the morphology of γ' particles during creep are unable to be directly analyzed.
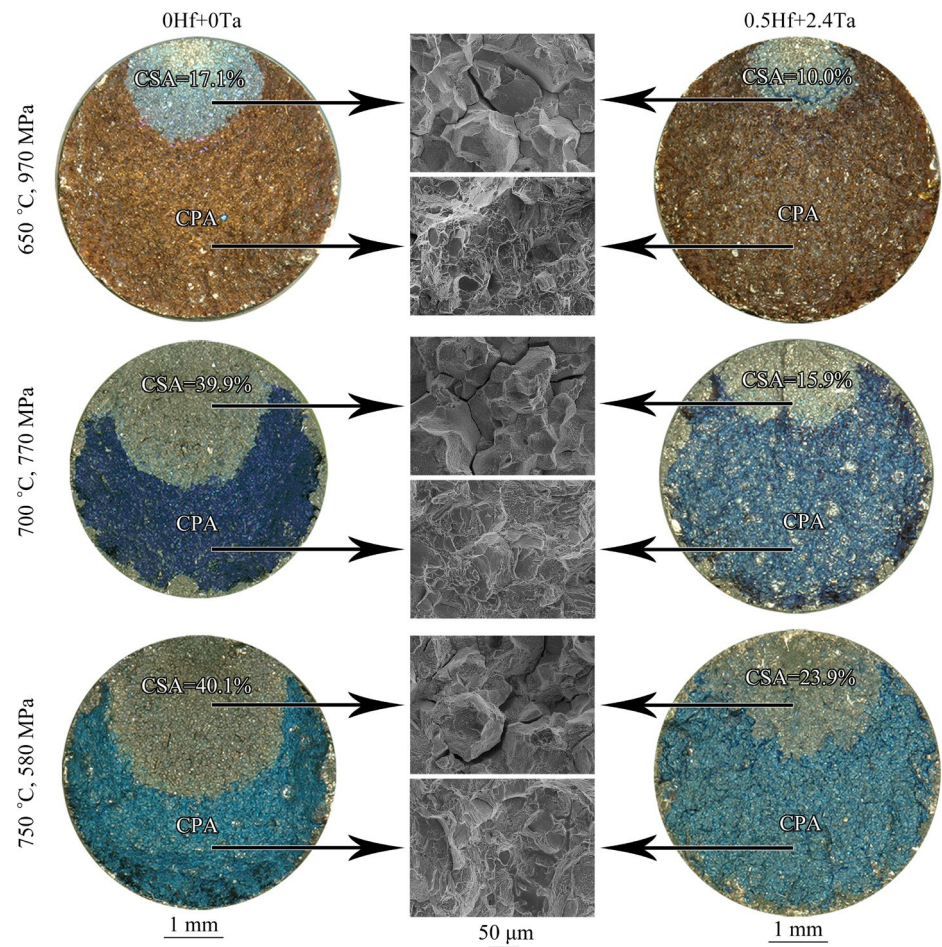
Fig. 5 Creep fractures of experimental alloys under different creep conditions (Area fractions of CSA are marked in images)
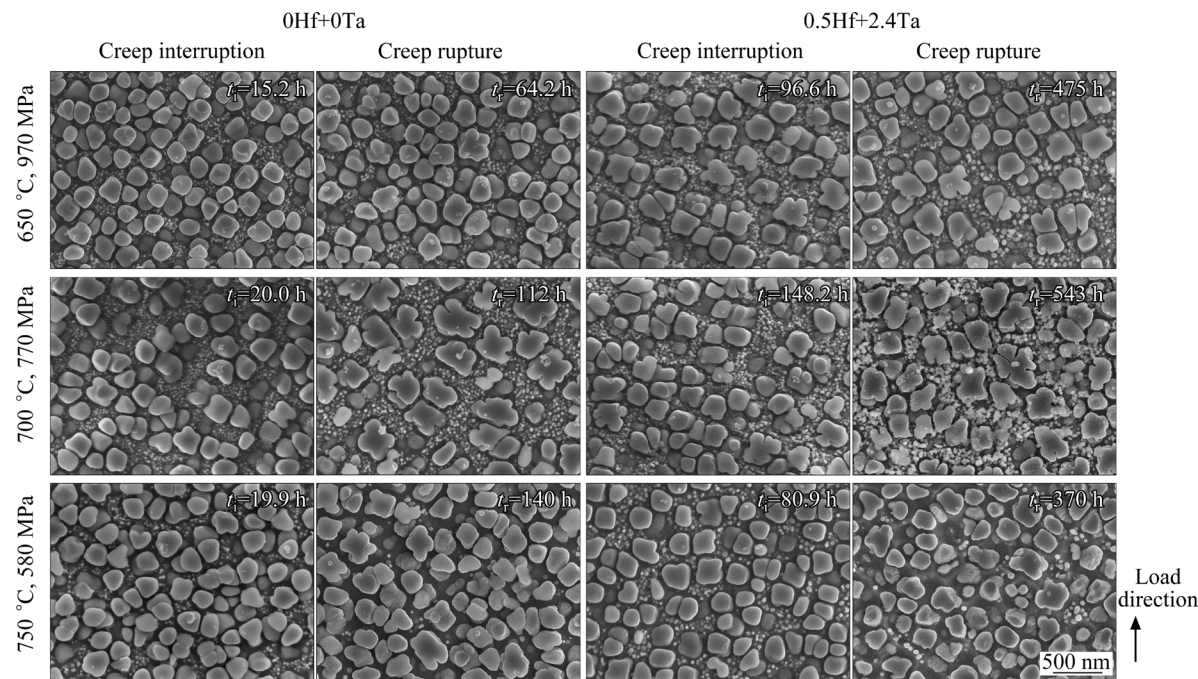
Fig. 6 Morphologies of γ' phase of experimental alloys after creep interruption and creep rupture under different creep conditions

4 Discussion

4.1 Effect of Hf and Ta on annealing twin boundaries after creep

EBSD boundary maps of experimental alloys after HT and creep under different conditions are shown in Fig. 7. Due to the angular resolution of EBSD being 1°−2° [17], the misorientation angle that is less than 2.5° is not included. Low-angle grain boundaries (2.5°≤θ<10°), high-angle grain boundaries (θ≥10°), and annealing twin boundaries (A-TBs) are represented by green, black, and red lines, respectively. A-TBs are characterized based on Brandon's criterion [18]. Because the creep strain of 0.5Hf+0Ta alloy after creep at 750 °C and 580 MPa is significantly higher as shown in Fig. 3 and the large creep deformation can promote the formation of low-angle grain boundaries [19], there are obviously more low-angle grain boundaries.

The statistical length fractions of annealing twin boundaries are plotted in Fig. 8. Firstly, the proportion of annealing twin boundaries in each alloy after creep is reduced compared to that after

HT. In addition to the reason mentioned above that creep deformation increases low-angle grain boundaries, it is also because creep deformation causes some annealing twin boundaries to lose their coherence with the matrix [16], and transforms them into random high-angle boundaries [20]. These two reasons together result in a decrease in the length fraction of annealing twin boundaries after creep. Secondly, Hf and Ta inhibit annealing twin boundaries after HT. The internal crystallographic crack initiation is closely related to the high fraction of annealing twin boundaries after HT [21]. Due to the addition of Hf and Ta, the content of carbides is increased, and carbides are transformed from distributed along PPBs to more uniformly distributed within grains [10]. It inhibits the annealing twin initiation and propagation, thus decreasing the fraction of annealing twin boundaries after HT [22]. Therefore, by inhibiting annealing twin boundaries after HT, Hf and Ta effectively suppress the initiation of cracks, thereby prolonging the creep rupture time. It is also worth noting that Hf and Ta do not always reduce the fraction of annealing twin boundaries after creep,
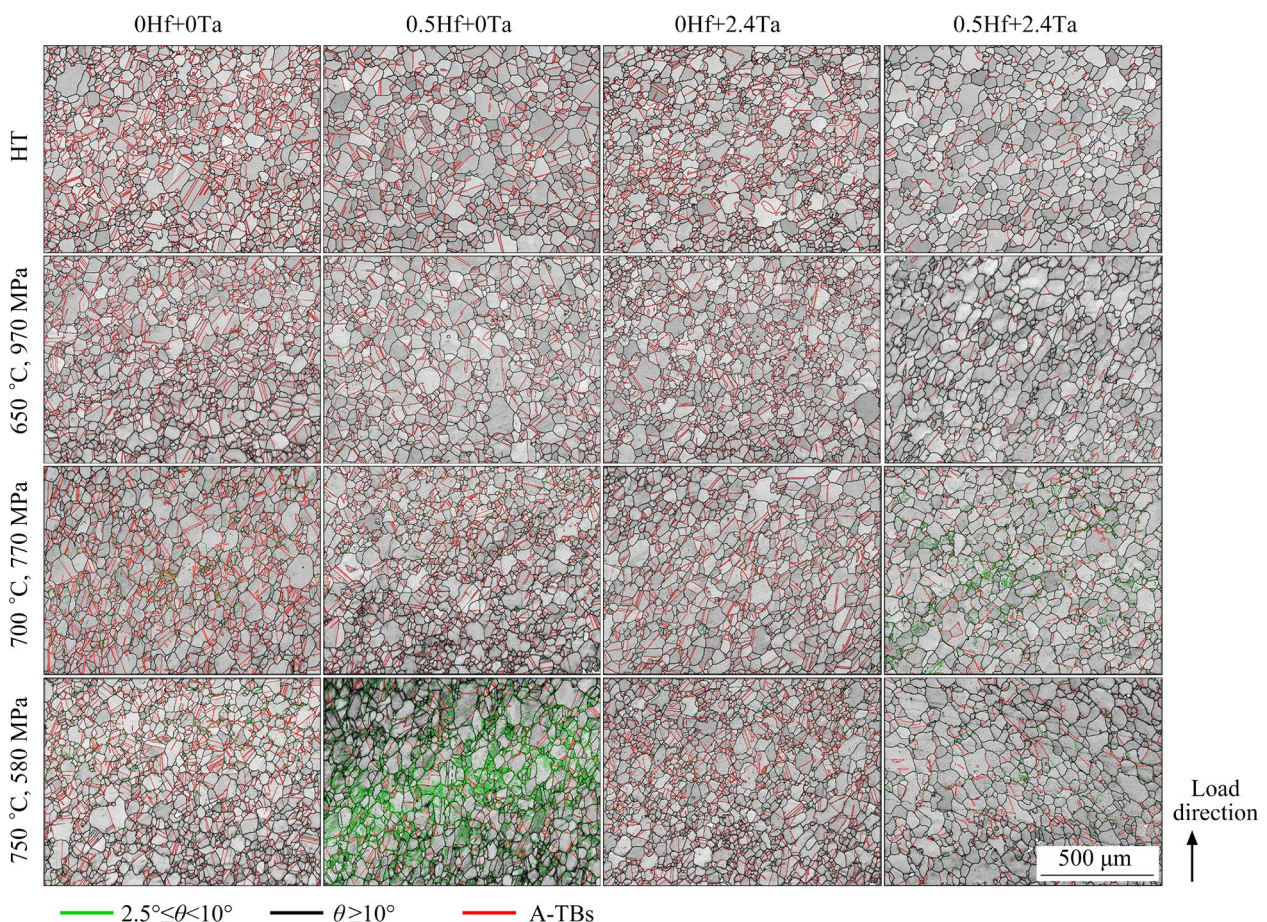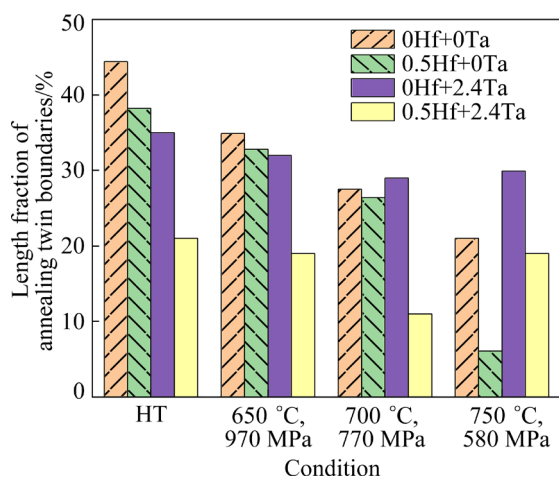

Fig. 7 EBSD boundary maps of experimental alloys after HT and creep under different conditions

Fig. 8 Length fraction of annealing twin boundaries of experimental alloys after HT and creep under different conditions

especially at 750 °C and 580 MPa. This is due to the significant difference in creep strain among alloys with different Hf and Ta contents at 750 °C and 580 MPa, as shown in Fig. 3, resulting in the influence of creep strain on annealing twin

boundaries exceeding the influence of Hf and Ta on annealing twin boundaries.

4.2 Effect of Hf and Ta on deformation substructures after creep

Figure 9 shows the typical deformation substructures of 0Hf+0Ta and 0.5Hf+2.4Ta alloys after creep interruption. After creep interruption at 650 °C and 970 MPa, extended stacking faults (ESFs) and microtwins (MTs) which sheared several secondary γ' precipitates and extended in the γ matrix are widely observed in both alloys, as shown in Figs. 9(a) and (b) indicated by red arrows. Figure 9(c) shows the high-resolution TEM image of an MT in the 0Hf+0Ta alloy. However, the extension of a large number of ESFs or MTs in the 0.5Hf+2.4Ta alloy is hindered, as shown in Fig. 9(b) indicated by yellow arrows. This is mainly due to three reasons: Firstly, the addition of Hf and Ta increases the volume fraction and equivalent particle size of secondary γ' precipitates, making the stacking faults extending more difficult. Secondly, the addition of Hf and Ta increases the lattice
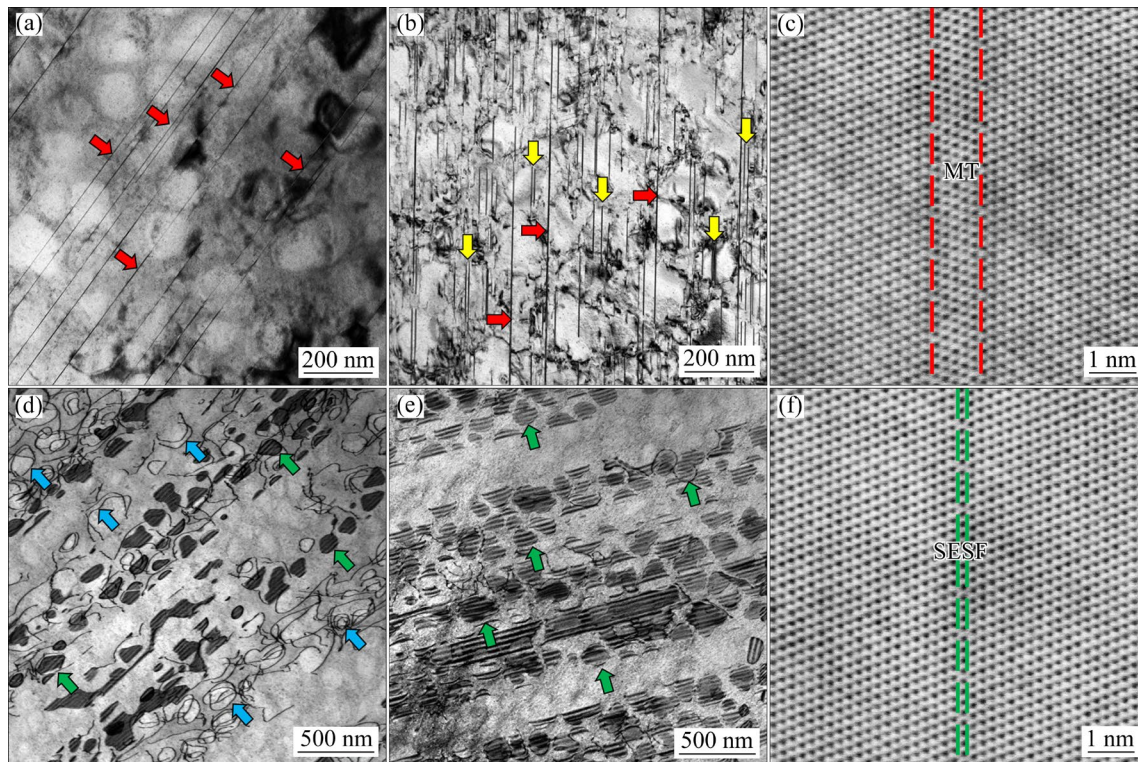
Fig. 9 Typical deformation substructures of experimental alloys after creep interruption (Beam direction (BD) is close to ⟨110⟩ zone axis): (a, b) TEM images of 0Hf+0Ta and 0.5Hf+2.4Ta alloys after creep interruption at 650 °C and 970 MPa, respectively; (c) High-resolution TEM image of MT in 0Hf+0Ta alloy; (d, e) TEM images of 0Hf+0Ta and 0.5Hf+2.4Ta alloys after creep interruption at 750 °C and 580 MPa, respectively; (f) High-resolution TEM image of SESF in 0Hf+0Ta alloy

mismatch of γ and γ' [10], and the interfacial dislocation networks generated by large lattice mismatch further hinder stacking faults extending [23]. Thirdly, Hf and Ta mainly enter the Al position of γ' phase and increase the stacking fault energy of γ' phase [24,25], thus increasing the required energy of the leading dislocation shearing γ' phase and forming ESFs and MTs. Therefore, the addition of Hf and Ta inhibits the extension of stacking faults. After creep interruption at 750 °C and 580 MPa, the dominated deformation mechanism changes to superlattice stacking faults (SSFs) shearing, as shown in Figs. 9(d) and (e) indicated by green arrows. Figure 9(f) shows the high-resolution TEM image of a superlattice extrinsic stacking fault (SESF) in the 0Hf+0Ta alloy. Due to the high creep temperature, a large number of matrix perfect dislocations bypass secondary γ' precipitates by dislocation climbing, as indicated by blue arrows. However, the dislocation climbing in the 0.5Hf+2.4Ta alloy is more difficult to observe. This is mainly because the addition of Hf and Ta reduces the stacking fault energy (SFE) of the γ matrix, making it easier for perfect dislocations to decompose into partial dislocations and generate stacking faults [11]. It increases the density of stacking faults in γ matrix and hinders the dislocation climbing. Therefore, the addition of Hf and Ta inhibits the dislocation climbing. The extending of stacking faults and dislocation climbing are the main sources of creep deformation, and they are inhibited by the addition of Hf and Ta. Therefore, Hf and Ta effectively decrease the minimum creep rate and delay the start time of the acceleration creep stage.

Figure 10 shows the typical deformation substructures of the 0.5Hf+2.4Ta alloy after creep at 650 °C and 970 MPa. Due to the reduction of SFE by the addition of Hf and Ta, the density of ESFs and MTs is increased in the 0.5Hf+2.4Ta alloy [11]. The intersecting position between ESFs and MTs and grain boundaries, or the intersecting position among ESFs and MTs has a higher dislocation density, as shown in Figs. 10(a) and (b), which is prone to the formation of creep cavities in the acceleration creep stage, promoting the transformation of secondary cracks from propagating along grain boundaries to propagating along ESFs and MTs inside grains, and thus the high density of ESFs and MTs can suppress the intergranular fracture [16]. In the 0.5Hf+2.4Ta alloy, some secondary cracks propagated along ESFs and MTs were observed, as shown in Fig. 10(c). It indicates the addition of Hf and Ta indeed suppresses the intergranular fracture by changing the crack propagation path, and because the intergranular damage is the main cause of creep rupture in the acceleration creep stage as mentioned in Section 3.3, Hf and Ta effectively prolong the creep rupture time.
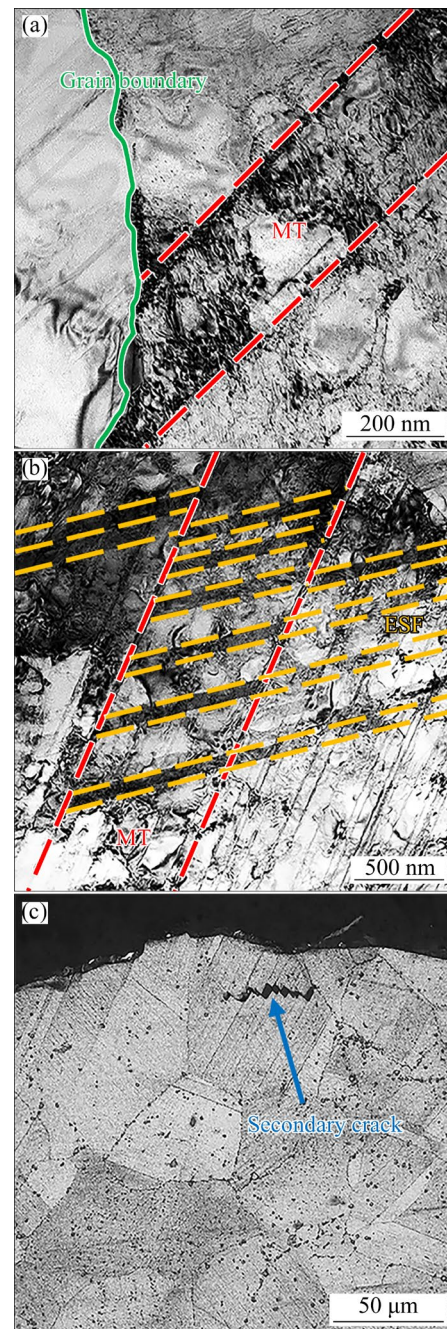
Fig. 10 Typical deformation substructures of 0.5Hf+2.4Ta alloy after creep at 650 °C and 970 MPa: (a) Intersection of MT and grain boundary; (b) Intersection of MT and ESFs; (c) Secondary crack propagated along ESFs and MTs

4.3 Effect of Hf and Ta on element segregation along stacking faults after creep

Alloying elements have a tendency to spontaneously segregate towards stacking faults, which is called Suzuki segregation [26]. The Suzuki segregation has been widely observed in many alloys, and it varies based on the alloying composition and the type of stacking faults [27−31]. In some alloys, chemically ordered localized phase transformation (LPT) occurs along stacking faults, which enhances the creep performances [32,33].

The Suzuki segregation of 0.5Hf+2.4Ta alloy is observed in Fig. 11. Figure 11(a) shows two stacking faults, where one superlattice stacking fault (SSF) is in the γ' precipitate, and the other stacking fault (SF) is in the γ matrix. EDS mapping and line scanning were performed on the area indicated by the yellow box in Fig. 11(a), and EDS results are shown in Fig. 11(b) and (c). Because the left side of the EDS scanning area is in the γ' precipitate and the right side is in the γ matrix, the contents of Ni, Al, Ti, Hf, and Ta on the left side are higher than those on the right side, while the contents of Co, Cr, and Mo on the left side are lower than those on the right side. But whether stacking faults are in the γ' precipitate or in the γ matrix, the depletion of Ni and Al and the enrichment of Co, Cr, Mo, Ti, Nb, and W along stacking faults are observed. It is worth noting that Ta also exhibits slight segregation along stacking faults, but Hf does not exhibit any obvious segregation.

To further investigate the Suzuki segregation of Hf and Ta and determine the occupancy of atoms in 0.5Hf+2.4Ta alloy, atomic level EDS mapping and line scanning were performed on a superlattice intrinsic stacking fault (SISF) in a γ' precipitate, and the radial Wiener filter was used for post processing, as shown in Fig. 12. The results are similar to those in Fig. 11. There are Ni, Al depletion and Ti, Co, W,
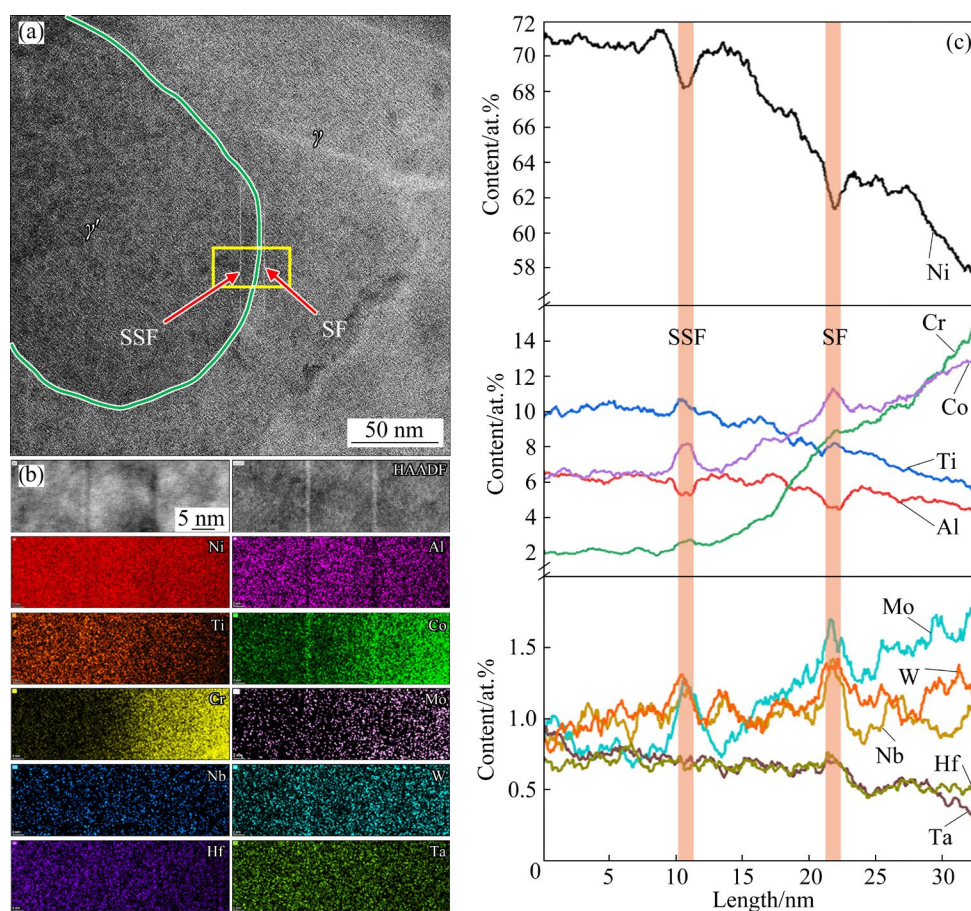
Fig. 11 Element segregation along stacking faults in 0.5Hf+2.4Ta alloy after creep interruption at 750 °C and 580 MPa: (a) High-angle annular dark-field (HAADF) image showing one stacking fault in γ' precipitate and the other stacking fault in γ matrix; (b) Bright-field (BF) image, HAADF image, and corresponding EDS net maps of area marked by yellow box in (a); (c) Corresponding EDS line scans data showing variation of element content with scanning length of area marked by yellow box in (a)
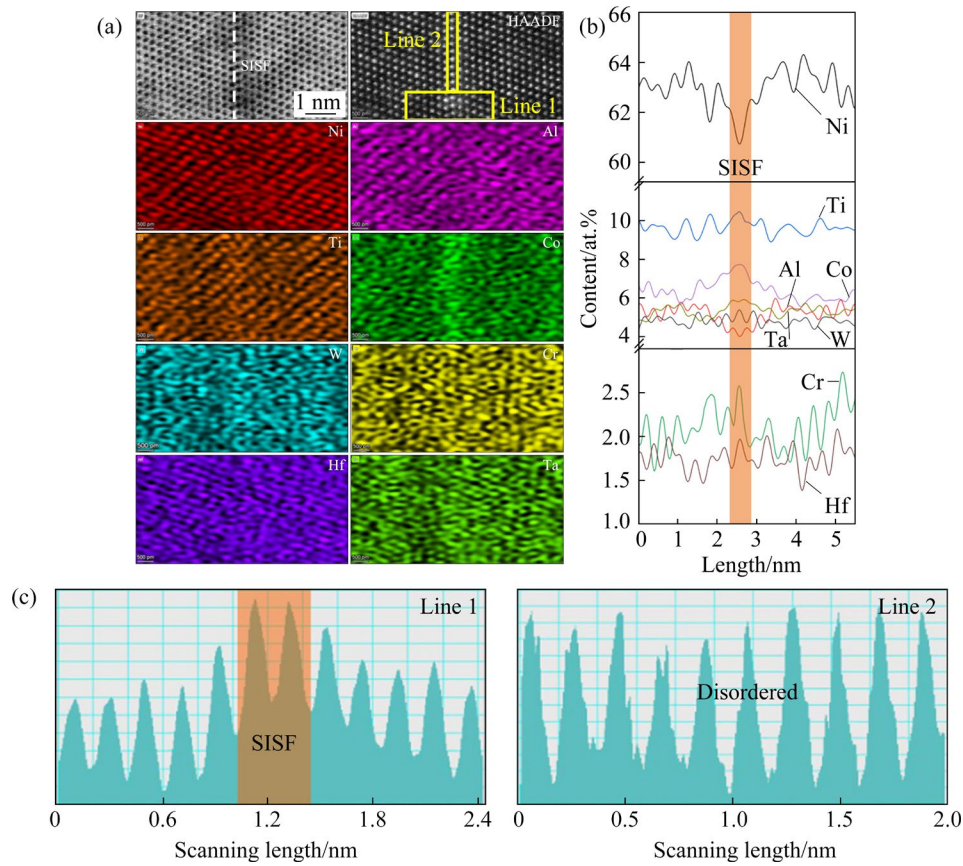
Fig. 12 STEM images along ⟨110⟩ zone axis, showing edge-on SISF in 0.5Hf+2.4Ta alloy after creep interruption at 750 °C and 580 MPa: (a) STEM-BF image, STEM-HAADF image, corresponding EDS net maps; (b, c) Corresponding EDS line scans and contrast intensity line scans showing variation of element content and contrast intensity of atomic sites with scanning length of area marked by yellow boxes in STEM-HAADF image of (a), respectively

Cr enrichment along the SISF, while Ta exhibits a slight segregation and Hf does not exhibit any obvious segregation along the SISF. Combined with the first-principles calculation results in Ref. [34], it can be inferred that Ti, W, Cr, and Ta mainly occupy Al sites, and Co mainly occupies Ni sites along stacking faults. Figure 12(c) shows the line scans of contrast intensity in the HAADF image of Fig. 12(a). Line 1 demonstrates that there is obvious element segregation along SISF, and Line 2 demonstrates that Suzuki segregation transforms the localized γ' phase into a disordered stacking fault phase along SISF [32,33]. Therefore, no chemically ordered LPT occurs along SISF after Hf and Ta addition. Compared with TSNA-1 [8] and ME501 [30] alloys which have chemically ordered LPT along SISF, it can be seen that to promote ordered LPT to further improve creep performances, in addition to adding Hf and Ta to the alloy, the adjustment of other elements contents such as Co, Cr, and Mo is also very crucial.

The Suzuki segregation of the 0Hf+0Ta alloy has been reported in the previous study [35], and it also shows the depletion of Ni and Al and the enrichment of Co, Cr, Mo, Ti, and Nb along stacking faults, but W does not exhibit an obvious segregation tendency. This difference in Suzuki segregation between 0Hf+0Ta and 0.5Hf+2.4Ta alloys allows us to reasonably infer that Ta promotes the Suzuki segregation of W in the 0.5Hf+2.4Ta alloy. Because Ta and W have lower diffusion coefficients compared to Co, Cr, Mo, Ti, and Nb [36,37], the Suzuki segregation of Ta and W contributes to suppressing further expansion and thickening of SSFs and MTs in γ' phase during the creep, thereby reducing the minimum creep rate [38].

5 Conclusions

(1) Hf and Ta prolonged the creep rupture time, delayed the start time of the acceleration creep stage,

and decreased the minimum creep rate, which significantly enhanced the creep performances.

(2) Hf and Ta reduced the length fraction of annealing twin boundaries after HT, which effectively suppressed the initiation of cracks, thereby prolonging the creep rupture time.

(3) Hf and Ta inhibited the extending of stacking faults and the dislocation climbing during the steady-state creep stage, thereby reducing the minimum creep rate and delaying the start time of the acceleration creep stag.

(4) Hf and Ta promoted the transformation of secondary cracks from propagating along grain boundaries to propagating along ESFs and MTs inside grains, which suppressed the intergranular fracture during the acceleration creep stage, thereby prolonging the creep rupture time.

(5) There was Suzuki segregation of Co, Cr, Mo, Ti, Nb, W, and Ta in 0.5Hf+2.4Ta alloy after creep, but no chemically ordered LPT occurred along stacking faults. Ta promoted the Suzuki segregation of W, further reducing the minimum creep rate.

(6) The combined addition of Hf and Ta can be considered in the composition design of novel PM Ni-based superalloys. However, further work is needed to determine the optimal amount of Hf and Ta addition and the adjustment of other elements.

CRediT authorship contribution statement

Hao-peng ZHANG: Writing – Original draft, Data curation, Methodology, Investigation, Visualization; **Jia-ming BAI:** Validation; **Xin-yu LI**, **Xiao-kun LI**, and **Jian JIA:** Resources; **Jian-tao LIU:** Resources, Funding acquisition; **Yi-wen ZHANG:** Resources, Conceptualization, Writing – Review & editing, Funding acquisition, Supervision.

Declaration of competing interest

The authors declare that they have no known competing financial interests or personal relationships that could have appeared to influence the work reported in this paper.

Acknowledgments

References

[1] XU Yuan-ming, ZHANG Shu-ming, HE Tian-peng, LIU Xin-ling, CHANG Xia-yuan. Prediction of low-cycle crack initiation life of powder superalloy FGH96 with inclusions based on damage mechanics [J]. Transactions of Nonferrous Metals Society of China, 2022, 32(3): 895−907.

[2] TAN Gang, LI Hui-zhong, WANG Yan, YANG Lei, QIAO Shi-chang, HUANG Zheng-qin, LIU Min-xue. Hot working characteristics of HEXed PM nickel-based superalloy during hot compression [J]. Transactions of Nonferrous Metals Society of China, 2020, 30(10): 2709−2723.

[3] YANG Le-biao, REN Xiao-na, GE Chang-chun, YAN Qing-zhi. Status and development of powder metallurgy nickel-based disk superalloys [J]. International Journal of Materials Research, 2019, 110(10): 901−910.

[4] LIU Feng, WANG Ze-xin, WANG Zi, ZHONG Jing, ZHAO Lei, JIANG Liang, ZHOU Run-hua, LIU Yong, HUANG Lan, TAN Li-ming, TIAN Yu-jia, ZEHNG Han, FANG Qi-hong, ZHANG Li-jun, ZHANG Li-na, WU Hong, BAI Li-chun, ZHOU Kun. High-throughput method–accelerated design of Ni-based superalloys [J]. Advanced Functional Materials, 2022, 32(28): 2109367.

[5] QIN Zi-jun, WANG Zi, WANG Yun-qiang, ZHANG Li-na, LI Wei-fu, LIU Jin, WANG Ze-xin, LI Zi-hang, PAN Jun, ZHAO Lei, LIU Feng, TAN Li-ming, WANG Jian-xin, HAN Hua, JIANG Liang, LIU Yong. Phase prediction of Ni-base superalloys via high-throughput experiments and machine learning [J]. Materials Research Letters, 2021, 9(1): 32−40.

[6] ZHANG H P, BAI J M, LI X Y, LI X K, JIA J, LIU J T, ZHANG Y W. Effect of Hf and Ta on creep rupture characteristics and properties of PM Ni-based superalloys [J/OL]. Acta Metallurgica Sinica. http://kns.cnki.net/kcms/detail/21.1139.tg.20230823.1034.010.html. (in Chinese)

[7] POWELL A, BAIN K, WESSMAN A, WEI D, HANLON T, MOURER D. Advanced supersolvus nickel powder disk alloy doe: chemistry, properties, phase formations and thermal stability [C]//Proc Superalloys 2016. Warrendale, PA: TMS, 2016: 189−197.

[8] SMITH T M, ZARKEVICH N A, EGAN A J, STUCKNER J, GABB T P, LAWSON J W, MILLS M J. Utilizing local phase transformation strengthening for nickel-base superalloys [J]. Communications Materials, 2021, 2(1): 106.

[9] ANTONOV S. Design of modern high Nb-content $\gamma-\gamma'$ Ni-base superalloys [M]. Illinois: the Illinois Institute of Technology, 2017.

[10] ZHANG H P, BAI J M, LI X K, LI X Y, JIA J, LIU J T, ZHANG Y W. Effect of hafnium and tantalum on the microstructure of PM Ni-based superalloys [J]. Journal of Materials Science, 2022, 57: 6803−6818.

[11] ZHANG H P, BAI J M, LI X K, LI X Y, JIA J, LIU J T, ZHANG Y W. Effect of Hf and Ta on the tensile properties of PM Ni-based superalloys [J]. Journal of Alloys and Compounds, 2023, 932: 167653.

[12] COCHARDT A W. High temperature alloys: US Patent,

3005705 [P]. 1961−10−24.

[13] ZHAO Y S, ZHANG J, LUO Y S, LI J, TANG D Z. Effects of Hf and B on high temperature low stress creep behavior of a second generation Ni-based single crystal superalloy DD11 [J]. Materials Science and Engineering: A, 2016, 672: 143−152.

[14] ZHANG Yi-wen, HU Ben-fu. Function of microelement Hf in powder metallurgy nickel-based superalloys [J]. Acta Metallurgica Sinica, 2015, 51(8): 967−975.

[15] YANG Zhi-kun, WANG Hao, ZHANG Yi-wen, HU Ben-fu. Effect of Ta content on high temperature creep deformation behaviors and properties of PM nickel base superalloys [J]. Acta Metallurgica Sinica, 2021, 57(8): 1027−1038.

[16] BAI J M, ZHANG H P, LI X Y, LIU J T, SUN Q S, LIU C S, ZHANG Y W. Evolution of creep rupture mechanism in advanced powder metallurgy superalloys with tantalum addition [J]. Journal of Alloys and Compounds, 2022, 925: 166713.

[17] HUMPHREYS F J. Characterisation of fine-scale micro-structures by electron backscatter diffraction (EBSD) [J]. Scripta Materialia, 2004, 51(8): 771−776.

[18] BRANDON D G. The structure of high-angle grain boundaries [J]. Acta Metallurgica, 1966, 14(11): 1479−1484.

[19] HIRATA T, OSA T, HOSOKAWA H, HIGASHI K. Effects of flow stress and grain size on the evolution of grain boundary microstructure in superplastic 5083 aluminum alloy [J]. Materials Transactions, 2002, 43(10): 2385−2391.

[20] KUANG Wen-jun, WAS G S, MILLER C, KAUFMAN M, ALAM T, GWALANI B, BANERJEE R. The effect of cold rolling on grain boundary structure and stress corrosion cracking susceptibility of twins in alloy 690 in simulated PWR primary water environment [J]. Corrosion Science, 2018, 130: 126−137.

[21] MIAO Jia-shi, POLLOCK T M, WAYNE JONES J. Crystallographic fatigue crack initiation in nickel-based superalloy René 88DT at elevated temperature [J]. Acta Materialia, 2009, 57(20): 5964−5974.

[22] TANG Yu-ling, LIU Jian-tao, CHENG Hong-wei, YU Hong-yao, ZHANG Yi-wen, ZHU Jing. Effect of hafnium on annealing twin formation in as-hot isostatically pressed nickel-based powder metallurgy superalloy [J]. Journal of Alloys and Compounds, 2019, 772: 949−954.

[23] ZHANG J X, WANG J C, HARADA H, KOIZUMI Y. The effect of lattice misfit on the dislocation motion in superalloys during high-temperature low-stress creep [J]. Acta Materialia, 2005, 53(17): 4623−4633.

[24] YANG Wen-chao, QU Peng-fei, SUN Jia-chen, YUE Quan-zhao, SU Hai-jun, ZHANG Jun, LIU Lin. Effect of alloying elements on stacking fault energies of γ and γ' phases in Ni-based superalloy calculated by first principles [J]. Vacuum, 2020, 181: 109682.

[25] HU Cheng-chao, ZHANG Zhao, CHEN Hui, HE Jian, GUO Hong-bo. Reactive elements dependence of elastic properties and stacking fault energies of γ-Ni, γ'-Ni₃Al and β-NiAl [J]. Journal of Alloys and Compounds, 2020, 843: 155799.

[26] SUZUKI H. Segregation of solute atoms to stacking faults [J]. Journal of the Physical Society of Japan, 1962, 17(2): 322−325.

[27] VISWANATHAN G B, SHI R, GENC A, VORONTSOV V A, KOVARIK L, RAE C M F, MILLS M J. Segregation at stacking faults within the γ' phase of two Ni-base superalloys following intermediate temperature creep [J]. Scripta Materialia, 2015, 94: 5−8.

[28] SMITH T M, ESSER B D, ANTOLIN N, CARLSSON A, WILLIAMS R E A, WESSMAN A, HANLON T, FRASER H L, WINDL W, MCCOMB D W, MILLS M J. Phase transformation strengthening of high-temperature superalloys [J]. Nature Communications, 2016, 7: 13434.

[29] SMITH T M, GOOD B S, GABB T P, ESSER B D, EGAN A J, EVANS L J, MCCOMB D W, MILLS M J. Effect of stacking fault segregation and local phase transformations on creep strength in Ni-base superalloys [J]. Acta Materialia, 2019, 172: 55−65.

[30] SMITH T M, ESSER B D, GOOD B, HOOSHMAND M S, VISWANATHAN G B, RAE C M F, GHAZISAEIDI M, MCCOMB D W, MILLS M J. Segregation and phase transformations along superlattice intrinsic stacking faults in Ni-based superalloys [J]. Metallurgical and Materials Transactions A, 2018, 49(9): 4186−4198.

[31] EGAN A J, XUE F, RAO Y, SPARKS G, MARQUIS E, GHAZISAEIDI M, TIN S, MILLS M J. Local phase transformation strengthening at microtwin boundaries in nickel-based superalloys [J]. Acta Materialia, 2022, 238: 118206.

[32] FENG Long-sheng, KANNAN S B, EGAN A, SMITH T, MILLS M J, GHAZISAEIDI M, WANG Yun-zhi. Localized phase transformation at stacking faults and mechanism-based alloy design [J]. Acta Materialia, 2022, 240: 118287.

[33] FENG Long-sheng, EGAN A, XUE Fei, MARQUIS E, MILLS M J, WANG Yun-zhi. Dynamic localized phase transformation at stacking faults during creep deformation and new criterion for superalloy design [J]. MRS Communications, 2022, 12: 991−1001.

[34] WU Qiong, LI Shu-suo. Alloying element additions to Ni₃Al: Site preferences and effects on elastic properties from first-principles calculations [J]. Computational Materials Science, 2012, 53(1): 436−443.

[35] ZHANG H P, BAI J M, LI X Y, LI X K, JIA J, LIU J T, ZHANG Y W. Segregation of alloying elements at planar faults during creep in the PM Ni-based superalloy FGH4096 [J]. Materials Letters, 2023, 349: 134741.

[36] CHEN Juan, ZHANG Li-jun, LU Xiao-gang. Diffusion behaviors of Rh, Ta, W, Re, Os and Ir in ternary L1₂−Ni₃Al alloys [J]. Intermetallics, 2018, 102: 11−20.

[37] WU Qiong, LI Shu-suo, MA Yue, GONG Sheng-kai. First principles calculations of alloying element diffusion coefficients in Ni using the five-frequency model [J]. Chinese Physics B, 2012, 21(10): 109102.

[38] KIM Y K, KIM D, KIM H K, OH C S, LEE B J. An intermediate temperature creep model for Ni-based superalloys [J]. International Journal of Plasticity, 2016, 79: 153−175.

Hf 和 Ta 对镍基粉末高温合金蠕变变形行为的影响

张浩鹏 [1,2]，白佳铭 [1,2,3]，李新宇 [1,2,3]，李晓鲲 [1,2]，贾 建 [1,2]，刘建涛 [1,2]，张义文 [1,2]

1. 钢铁研究总院 高温材料研究所，北京 100081；
2. 北京钢研高纳科技股份有限公司，北京 100081；
3. 东北大学 材料科学与工程学院，沈阳 110819

摘 要：对 4 种不同 Hf 和 Ta 含量的镍基粉末高温合金分别在 650 ℃、970 MPa，700 ℃、770 MPa 和 750 ℃、580 MPa 下进行蠕变试验。采用扫描电子显微镜、电子背散射衍射和球差校正扫描透射电子显微镜研究 Hf 和 Ta 对该合金蠕变变形行为的影响。结果表明，Hf 和 Ta 在加速蠕变阶段抑制了沿晶断裂和裂纹萌生，从而延长了蠕变断裂时间。Hf 和 Ta 在稳态蠕变阶段抑制了层错扩展和位错攀移，促进了 W 的铃木偏聚，从而降低了最小蠕变速率和推迟了加速蠕变阶段的开始时间。添加 Hf 和 Ta 后，观察到 Co、Cr、Mo、Ti、Nb、W 和 Ta 沿层错的铃木偏聚，这导致 γ' 相中发生微区相变，而且层错相是化学无序的。本研究为新型镍基粉末高温合金的成分设计提供了思路，为 Hf 和 Ta 的共同添加提供了理论依据。

关键词：镍基粉末高温合金；铪；钽；蠕变变形行为；铃木偏聚

(Edited by Wei-ping CHEN)